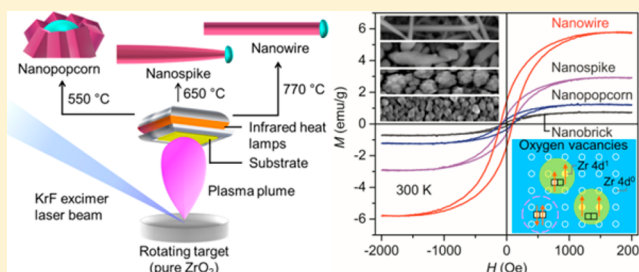# Defect-Rich Dopant-Free ZrO$_2$ Nanostructures with Superior Dilute Ferromagnetic Semiconductor Properties

Md Anisur Rahman, S. Rout, Joseph P. Thomas, Donald McGillivray, and Kam Tong Leung*

WATLab and Department of Chemistry, University of Waterloo, Waterloo, Ontario N2L 3G1, Canada

S *Supporting Information*

ABSTRACT: Control of the spin degree of freedom of an electron has brought about a new era in spin-based applications, particularly spin-based electronics, with the potential to outperform the traditional charge-based semiconductor technology for data storage and information processing. However, the realization of functional spin-based devices for information processing remains elusive due to several fundamental challenges such as the low Curie temperature of group III−V and II−VI semiconductors (<200 K), and the low spin-injection efficiencies of existing III−V, II−VI, and transparent conductive oxide semiconductors in a multilayer device structure, which are caused by precipitation and migration of dopants from the host layer to the adjacent layers. Here, we use catalyst-assisted pulsed laser deposition to grow, for the first time, oxygen vacancy defect-rich, dopant-free ZrO$_2$ nanostructures with high T_C (700 K) and high magnetization (5.9 emu/g). The observed magnetization is significantly greater than both doped and defect-rich transparent conductive oxide nanomaterials reported to date. We also provide the first experimental evidence that it is the amounts and types of oxygen vacancy defects in, and not the phase of ZrO$_2$ that control the ferromagnetic order in undoped ZrO$_2$ nanostructures. To explain the origin of ferromagnetism in these ZrO$_2$ nanostructures, we hypothesize a new defect-induced bound polaron model, which is generally applicable to other defect-rich, dopant-free transparent conductive oxide nanostructures. These results provide new insights into magnetic ordering in undoped dilute ferromagnetic semiconductor oxides and contribute to the design of exotic magnetic and novel multifunctional materials.

INTRODUCTION

Modern solid-state electronics is often developed in parallel with or directly through the evolution of structures based on their "champion" materials. The revolutions of microelectronics with Si, optoelectronics with GaAs, and display technology with liquid crystals are some of many examples. These conventional applications are based mainly on manipulating the electron charge. An intriguing alternative is the field of spin-based electronics, in which the manipulation of the electron spin in semiconductor devices promises a variety of emerging applications, such as nonvolatile memory, quantum computing, and solid-state magneto-optical telecommunication devices.[1] The success of spin-based electronics depends on establishing a champion material that combines the desirable properties of a ferromagnet with those of a semiconductor. Dilute ferromagnetic semiconductors belong to one such unique class of materials in which the semiconducting and ferromagnetic properties are combined in a single material.[2] The existing techniques for fabricating semiconductor heterostructures enable incorporation of dilute ferromagnetic semiconductor layers into transistors, quantum wells, and other electro-optical devices, in which spin splitting can also be tuned by confinement energy and size quantization.[3,4] The manipulation of the electron spin in dilute ferromagnetic semiconductor devices promises higher speed, higher storage capacity, more efficiency, and lower power consumption in a wide range of applications including magnetic storage, magnetic memories, quantum computers, quantum communication, sensors, and other information and communications technology devices.[1] Furthermore, in contrast to magnetic semiconductors, dilute ferromagnetic semiconductors offer reliable control of not just stoichiometry but also the nature of carrier, impurity, and crystallographic structure, which can be used to provide desirable magneto-optical and transport properties.[5]

For dilute ferromagnetic semiconductors, the Ga$_{1−x}$Mn$_x$As and In$_{1−x}$Mn$_x$As systems have attracted the most attention.[5] These systems have provided a fertile ground to demonstrate spin injection, control of ferromagnetism by means of the electric field, and tunneling anisotropic magnetoresistance in planar junctions.[6] As only ferromagnets with Curie temperature (T_C) > 500 K are qualified for use in a room-temperature device,[7] their low T_C (<200 K)[5] becomes their main drawback for practical device applications. In contrast, transparent dilute ferromagnetic semiconductor oxides (TDFSOs) have generally higher T_C, with, e.g., 850−930 K reported for Cr-doped indium oxide thin film.[8] TDFSOs therefore represent the alternative materials for future applications in spin-based electronics.

There are, however, major challenges in the development of dopant-based TDFSO systems, which include the low solubility limit of transition metal ion dopants (such as Mn, Fe, Co, and Cr) in the host lattice, and their tendency to form clusters and to occupy sites other than the cation-substitutional ones.[9] While the resulting systems may have collective magnetic property, the magnetism is often not uniform over the entire materials due to dopant inhomogeneity. More importantly, the dopants in a multilayer device structure have been found to migrate from the host layer to the adjacent layers during operation of the device.[10] The elusive nature of dopants has therefore made practical implementation difficult.

Studies employing X-ray magnetic circular dichroism have further revealed that dopants (Co, Mn, and Cr) with unpaired d electrons are not the origin of ferromagnetism, rather it is the dopant-induced defects that contributes to ferromagnetism.[11,12] In more recent studies, ferromagnetism has also been observed in oxygen-vacancy-rich nanocrystalline TDFSOs that nominally do not contain any magnetic impurity.[13,14] This begs the question of whether ferromagnetism is really due to just extrinsic effects such as doping and secondary phases, or it also has an intrinsic origin. While traditional mechanisms of ferromagnetism, such as phase segregation, superexchange, and double exchange, cannot readily account for the long-range ordering in doped TDFSOs,[15] improved models involving bound magnetic polaron[7] and charge transfer ferromagnetism[16] have also failed to address the fundamental question of how pure semiconducting oxides, i.e., without any transition metal dopants (d electrons), can become ferromagnetic.

Clearly, there is an acute need for an alternative approach to the traditional method of incorporating dopants as a means to create the desirable properties of TDFSOs. In order to better understand and to exploit the spin-dependent properties of TDFSOs in spin-based electronic devices and other applications, it is crucial to prepare dopant-free TDFSOs in which ferromagnetic ordering can be controlled at or above the room-temperature by the amount of oxygen vacancy defects. For defect-rich undoped TDFSOs, there are additional challenges. The traditional method of defect creation that involves post-treatment of as-grown stoichiometric structures in a reductive environment could, however, only produce exterior defects and the resulting low magnetization (0.4 emu/g)[14] also seriously hinders the development of spin-based multifunctional devices. Compared to thin films, one-dimensional (1D) nanostructures, such as nanowires or nanospikes, with relatively large specific surface area offer abundant surface defects that could potentially enhance the intrinsic ferromagnetism. 1D nanostructures also offer unique, physical properties arising from the nanoscale size and quantum confinement effects, all of which could affect carrier transport, exchange interaction of electron spins, and therefore ferromagnetic properties. More importantly, the origin of ferromagnetic properties in undoped TDFSO nanostructures with a large specific surface area (such as nanospikes and nanowires) and different compositions of (singly charged, double charged, and neutral) oxygen vacancy defects[17] remains unknown. Nanostructures with a large amount of oxygen vacancy defects (both at the surface and in the bulk of the nanostructure) are therefore expected to provide an excellent platform to investigate the origin of ferromagnetism in undoped TDFSOs.

As a case study, we have chosen ZrO_2, because similar to other TDFSOs, conflicting origin of ferromagnetism, including oxygen vacancy defects,[13] and magnetic[18] and nonmagnetic

dopants,[19] have been proposed for ZrO_2 thin films. As a high-κ dielectric, there is also intense interest to use ZrO_2 to replace SiO_2 as the gate insulators for silicon devices due to the high leakage current of SiO_2 layer below 10 nm thickness.[20] Understanding the defect-related properties of ZrO_2 is therefore extremely important for future metal oxide semiconductor transistors and spin-electronic devices. Here, we have prepared, for the first time, oxygen vacancy defect-rich (both at the surface and in the bulk), dopant-free nanostructures of ZrO_2 with different specific surface areas and defect compositions, including nanobricks, nanopopcorns, nanospikes, and nanowires, on a Si substrate by catalyst-assisted pulsed laser deposition (PLD) method. We show that ferromagnetism is independent of the phase of ZrO_2, and is directly related to the specific surface area of the nanostructure and to the amounts and types of oxygen vacancy defects in that particular nanostructure. A remarkably high saturation magnetization (5.9 emu/g at 2000 Oe) and a high T_C (700 K) are observed for ZrO_2 nanowires. To explain the origin of ferromagnetism, we hypothesize a new defect-induced bound polaron model, in which the exchange interactions of singly charged and doubly charged oxygen vacancy defects and reduced Zr $4d^1$ ions lead to the formation of bound magnetic polarons, and the percolation of these polarons results in the observed ferromagnetism. Our results therefore not only firmly establish oxygen vacancy defects are primarily responsible for the origin of ferromagnetism in undoped TDFSO nanostructures, but also demonstrate the potential of controlling their magnetic properties by manipulating the composition of oxygen vacancy defects within the host lattice.

■ MATERIALS AND METHODS

ZrO_2 nanostructures are synthesized on oxidized Si(100) template by catalyst-assisted pulsed laser deposition (PLD) method in a NanoPLD system (PVD Products) with a base pressure of 1×10^{-7} Torr. A KrF excimer laser (248 nm wavelength) operated with a laser fluence of 350 mJ/pulse at a repetition rate of 5 Hz is used to ablate a ZrO_2 target, prepared by cold-pressing ZrO_2 powders (Aldrich, 99.99% purity) with a pressure of 25 MPa followed by sintering at 1000 °C in air for 48 h. A silicon chip (10 × 10 mm², 525 μm thick), precut from a Si(100) wafer (p-type, B-doped, with a resistivity of <0.005 Ω cm, Siegert Wafer), is chemically oxidized using H_2O_2 and NH_4OH solutions following the RCA cleaning procedure.[21] The resulting oxidized Si(100) substrate (denoted as Ox-Si) is used to support gold nanoisland (GNI) catalysts, which are produced by magnetron sputtering a thin layer of Au followed by annealing in air. The GNI/Ox-Si template is mounted perpendicular to the expansion direction of the laser plume on a windowed substrate holder. During deposition, the substrate is in close proximity to the top of the visible region of the laser plume, with the target-to-substrate separation kept at 30 mm. The substrate temperature (i.e., growth temperature) can be varied between 550 and 770 °C by radiative heating of infrared heat lamps from the backside of the substrate. Deposition is carried out on the GNI/Ox-Si template for 90 min in 200 mTorr of Ar at a flow rate of 10 sccm.

The morphology of the sample is examined by field-emission scanning electron microscopy (SEM) in a Zeiss Merlin microscope. Glancing-incidence X-ray diffraction (XRD) measurements are performed in a PANalytical MRD X'pert Pro diffractometer with a Cu Kα source, by using a parallel X-ray beam setup with an incidence angle of $\omega = 0.3°$ over the selected 2θ range. The crystallinity of ZrO_2 nanostructures is studied by transmission electron microscopy (TEM) in a Zeiss Libra 200MC microscope. For TEM measurement, the nanostructures are scraped off the substrate using a sharp blade and mixed with liquid-chromatography-grade methanol in an Eppendorf tube and sonicated for 10 min, and the resulting suspension is then

transferred onto a holey carbon TEM copper grid. The chemical-state compositions of the nanostructures are analyzed by X-ray photoelectron spectroscopy (XPS) in a Thermo-VG Scientific ESCALab 250 microprobe with a monochromatic Al Kα X-ray source (1486.6 eV), operated with a typical energy resolution of 0.4−0.5 full width at half-maximum. The magnetic property is characterized at different temperature by using a superconducting quantum interference device (SQUID) magnetometer (Quantum Design MPMS SQUID-VSM), with the applied magnetic field direction parallel to the sample surface. It should be noted that only plastic tweezers and quartz holders have been used during sample preparation and magnetic measurement to avoid any unintentional ferromagnetic contamination. The diamagnetic contribution from the Si substrate and the quartz sample holder has been removed, and the magnetization of the ZrO_2 nanostructures is normalized by the mass of the measured sample, as estimated by assuming that the nanostructures are completely filled in the measured volume (i.e., without considering the filling factor) with a bulk density of 5.68 g/cm^3.

■ RESULTS AND DISCUSSION

Synthesis and Characterization of ZrO_2 Nanostructures. The SEM images shown in Figure 1 illustrate the PLD growth of ZrO_2 nanostructures on an oxidized Si template decorated with gold nanoislands (GNI/Ox-Si). For all the depositions, gold nanoislands (GNIs) have been deposited on the oxidized Si (Ox-Si) substrate for the same amount of sputtering time (4 s) followed by annealing under the same conditions (at 600 °C in air for 30 min). The resulting GNI size distributions are found to be highly reproducible, with a mean diameter of 10−20 nm (Figure 1a). The thickness of the SiO_2 layer has also increased correspondingly from 3 nm after the RCA cleaning[21] to 6 nm for the GNI/Ox-Si template. PLD growth on the GNI/Ox-Si template in 200 mTorr Ar for 90 min at 550 °C evidently produces ZrO_2 nanopopcorns, made up of distorted tetragonal-shaped nanobricks (Figure 1c1, inset). Each nanotetragon has well-defined facets with typical lengths of 15−30 nm, and their bases are joined to one another around a GNI as their common core in a flower-like morphology (Figure 1c2, inset). On the other hand, deposition at 650 °C produces spike-like nanostructures (Figure 1d1), the length and the base diameter of which are estimated to be several hundred nm and 40−50 nm, respectively (Figure 1d2). The backscattered-electron image further reveals its sharp tip with a diameter less than 10 nm, on top of which lies a gold nanoparticle (Figure 1d2, inset). This confirms that the GNI catalysts have been detached from the substrate, and they stay on top of the growing nanostructures, clearly following the vapor liquid solid (VLS) nanostructure growth mechanism.[22] Interestingly, PLD growth at 770 °C produces slightly tapered nanowires with a nearly uniform cross section, the diameter of which decreases from 50 to 60 nm at the base to 40−50 nm at the tip along their typical lengths of 2−3 μm (Figures 1e1, 1e2). As for the nanospikes, the presence of Au nanoparticles at the tips of individual nanowires also supports the VLS growth mechanism for these nanowires.

In a separate experiment, we perform PLD growth of ZrO_2 without the GNI catalysts on the Ox-Si substrate. Figure 1b shows that this leads to a nanoparticulate film with nanobricks of typical lengths of 10−30 nm. Closer examination of the nanostructured films shown in Figures 1c−1e also reveals the presence of similar type of nanobricks among the bases of the nanopopcorns, nanospikes and nanowires. This suggests a concurrent vapor−solid growth mechanism in regions where there is no catalyst. However, PLD growth at 550−750 °C on a
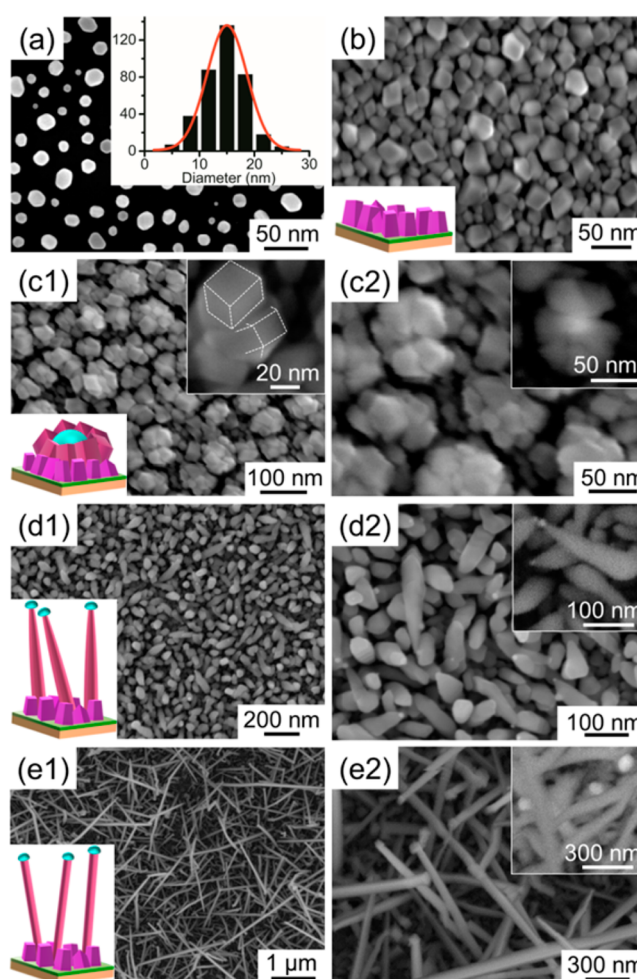

Figure 1. SEM images of (a) typical gold nanoislands (GNIs), with the corresponding near-Gaussian size distribution (inset), deposited on an Ox-Si template, (b) ZrO_2 nanobrick film PLD-grown on pristine Ox-Si template (without any GNI) at 770 °C, ZrO_2 nanopopcorn, nanospike and nanowire films PLD-grown on the GNI/Ox-Si templates in 200 mTorr Ar for 90 min at, respectively, (c1, c2) 550 °C, (d1, d2) 650 °C, and (e1, e2) 770 °C. The corresponding lower left insets show schematic models of the respective as-grown nanostructures, with the backscattered electron images (upper right insets) depicting a gold nanoparticle (c2) at the core and (d2, e2) at the tips of the respective nanostructures. The SEM image in the upper right inset of (c1) illustrates the shape of the ZrO_2 nanopopcorns.

GNI/Ox-Si template with the SiO_2 layer thickness less than 6 nm produces mainly nanopopcorn-like film (not shown), due to the formation of Au-silicide by interfacial reaction of Au and Si.[23] The thicker SiO_2 layer on the Ox-Si template prevents Au diffusion and the subsequent Au-silicide formation. A SiO_2 layer with the appropriate thickness (of at least 6 nm) is therefore extremely important for enabling VLS growth in the present PLD method.

In the present study, the growth temperatures chosen for the nanostructures are all lower than the lowest eutectic temperature for the bulk Au−Zr binary system (863 °C).[24] The formation of shorter tapered-shape nanospikes at 650 °C and of longer nanowires at 770 °C therefore suggests that the catalysts remain semisolid below 650 °C, which consequently reduces the diffusion rate of incoming atoms through the Au seeds and thus the VLS growth rate. As a result, VLS growth becomes less dominant below 650 °C. The smaller average diameter found

for the nanowires than the nanospikes also suggests that the VLS growth rate is higher than the vapor—solid growth rate at a particular growth temperature above 650 °C. The present observation therefore illustrates that the PLD growth temperature can be used to effectively manipulate the dominant growth mode (vapor—solid vs VLS), and consequently the cross-sectional dimension and overall morphology of the deposited ZrO_2 nanostructures. In Figure 2, we schematically summarize the different ZrO_2 nanostructures on the two templates: Ox-Si and GNI/Ox-Si, obtained at three different growth temperatures.
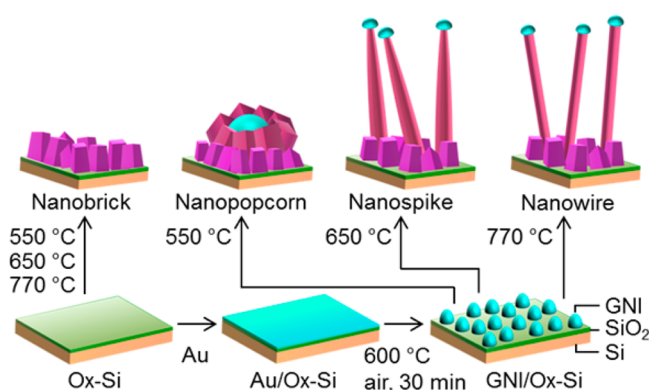
Figure 2. Schematic models of ZrO_2 nanostructures grown on Ox-Si templates without and with gold nanoislands (GNIs) in 200 mTorr Ar for 90 min at 550 °C, 650 °C, and 770 °C.

Figure 3 shows the corresponding glancing-incidence X-ray diffraction (XRD) patterns of the as-deposited nanostructures.
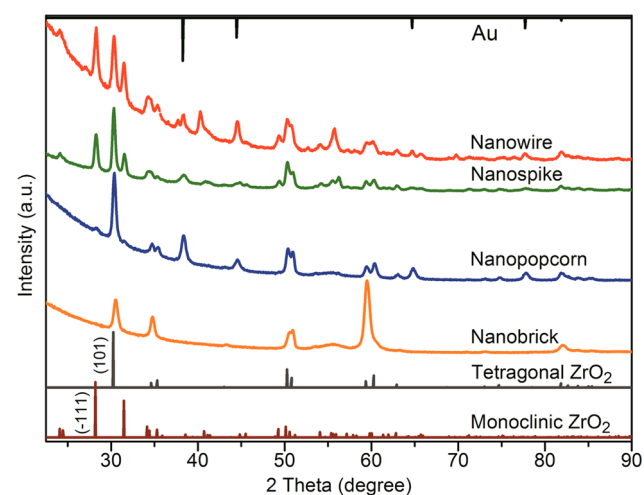

Figure 3. Glancing-incidence XRD patterns of different PLD-grown ZrO_2 nanostructured films obtained at an incidence angle of 0.3°. The PDF2 reference patterns of the FCC phase of Au (#03−065−8601), and of the monoclinic phase (#01−083−0940) and tetragonal phase (#01−080−0784) of ZrO_2 are shown as top, and bottom bar graphs, respectively.

The prominent diffraction peaks of the nanobrick film are in excellent accord with the tetragonal ZrO_2 reference pattern (PDF2 #01−080−0784). For nanopopcorns, additional minor contributions from the monoclinic ZrO_2 features (PDF2 #01−083−0940), along with the features from the FCC phase of metallic Au (PDF2 #03−065−8601), are observed. These

additional contributions from the monoclinic ZrO_2 features are found to increase for the nanospikes and nanowires. Of particular interest are the remarkably different relative peak intensity ratios of the monoclinic (−111) peak at 28.18° to the tetragonal (101) peak at 30.24° among the nanopopcorns, nanospikes, and nanowires.

Further insight into the morphology and crystallography of the as-deposited nanostructures can be obtained by transmission electron microscopy (TEM). Figure 4a1 shows a
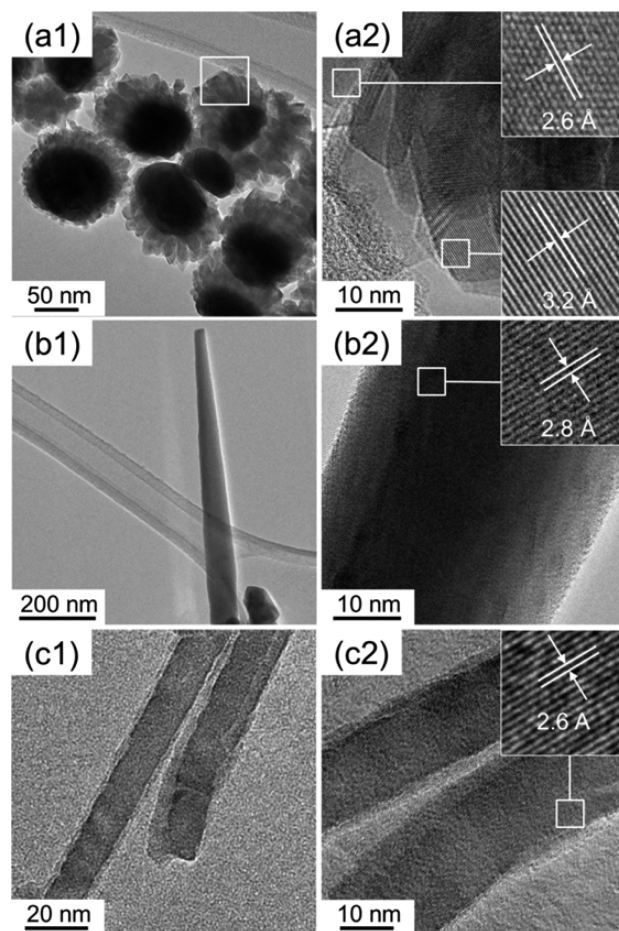
Figure 4. TEM images of typical (a1, a2) ZrO_2 nanopopcorns, (b1, b2) nanospikes, and (c1, c2) nanowires, with the corresponding high-resolution images of selected areas of individual nanostructures shown in insets.

typical low-magnification TEM image of the ZrO_2 nanopopcorns, in which clustering of several distorted nanotetragons (gray region) around a single gold nanoparticle core (dark region) is clearly observed without any evidence of gold at the edge of these tetragons. Figure 4a2 shows the high-resolution TEM image of two selected areas of a nanopopcorn. The lattice fringes of the nanotetragons at the perimeter indicate that the constituent particles are single-crystalline, and that their respective interplanar spacings of 3.2 and 2.6 Å correspond to those of the (−111) and (002) planes of monoclinic ZrO_2. In Figure 4b1, the tapered shape of the nanospikes is clearly observed, while the diameter of the nanowires appears nearly uniform along the entire length as shown in Figure 4c1. The corresponding high-resolution TEM images (Figures 4b2, 4c2) show that the nanospikes and nanowires are also single-crystalline and that their respective interplanar spacings of 2.8
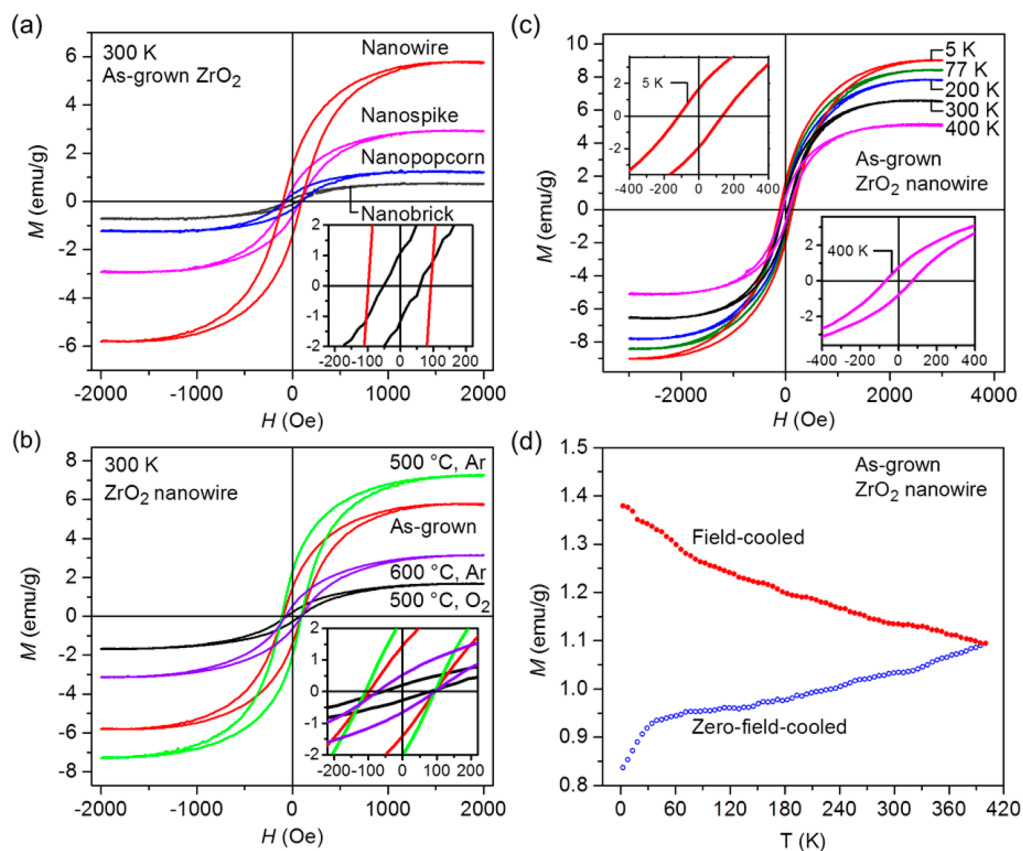
Figure 5. (a) Magnetization (M) vs magnetic field (H) curves of as-grown ZrO_2 nanostructured films, with the enlarged view of the hysteresis loops for ZrO_2 nanobrick and nanowire films given in inset. (b) $M−H$ curves for as-grown and annealed ZrO_2 nanowire films under different post-treatment conditions of annealing temperature and atmosphere, with the enlarged view of the respective hysteresis loops given in inset. (c) $M−H$ curves for the as-grown ZrO_2 nanowire film measured at 3000 Oe for temperature (T) = 5, 77, 200, 300, and 400 K. The insets show the magnified hysteresis loops near the origin at 5 and 400 K. (d) Magnetization as a function of temperature for the as-grown ZrO_2 nanowire film following field-cooled and zero-field-cooled measurements at H = 100 Oe.

and 2.6 Å correspond to the (111) and (002) planes of bulk monoclinic ZrO_2, respectively. Interestingly, the nanobricks in the gaps among the nanopopcorns, nanospikes and nanowires exhibit interplanar spacings of 2.9 and 2.5 Å, corresponding to the (101) and (110) planes of tetragonal ZrO_2, respectively (Figure S1). These results therefore suggest that the PLD-grown ZrO_2 nanopopcorns, nanospikes, and nanowires are predominantly monoclinic, while the nanobricks among these nanostructures (similar to those that make up the nanobrick film) are predominantly tetragonal ZrO_2.

Magnetic Property of ZrO_2 Nanostructures. Figure 5a shows the room-temperature magnetization versus magnetic field ($M−H$) curves for the nanobricks, nanopopcorns, nanospikes, and nanowires when the external magnetic field is applied parallel to the respective sample surfaces (i.e., in-plane direction). Evidently, all the samples exhibit well-defined hysteresis loops, indicating room-temperature ferromagnetic behavior. More importantly, the film containing more monoclinic phase has a larger saturation magnetization. The saturation magnetization (M_S) measured at 2000 Oe for the nanowires (5.9 emu/g) is found to be 2.0, 4.9, and 9.8 times those of nanospikes (2.9 emu/g), nanopopcorns (1.2 emu/g), and nanobricks (0.6 emu/g), respectively, while the coercivity (H_C) for the nanowires (99 Oe) is approximately twice that of the nanobricks (50 Oe) (Figure 5a, inset). This is a significant result, because in marked contrast to the previously reported ZrO_2 planar thin films,[13,25] of which the observed ferromag-

netic behavior was found to reduce with increased amount of the monoclinic phase, we observe increase in ferromagnetism with increase of the monoclinic phase in the ZrO_2 nanostructures here. It should be noted that we also characterize and obtain essentially diamagnetic behavior for the pristine Ox-Si template, GNI/Ox-Si template, and quartz sample holder (used for the magnetization measurements) under the same conditions (not shown). In addition, to investigate the effect of the PLD growth temperature on the magnetization of these substrates, we examine pristine Ox-Si substrates annealed in 200 mTorr Ar at 770 °C for 90 min in the PLD chamber and confirm that they also do not exhibit any ferromagnetic behavior. In addition, the magnetic properties of the as-grown ZrO_2 nanowires could be improved further by annealing in a reductive environment, with detailed discussion about Figure 5b given in the next section.

We also characterize the magnetic properties of as-grown ZrO_2 nanowires at four other temperatures, T = 5, 77, 200, and 400 K (Figure 5c). The presence of well-defined hysteresis loops supports strong ferromagnetic behavior over the entire temperature range, from 5 K to as high as 400 K (the maximum sampling temperature supported by our SQUID magneto-meter). The coercivity (68 Oe), remanence (0.8 emu/g), and saturation magnetization (5.1 emu/g) observed at 400 K have nearly doubled, respectively, to 115 Oe, 1.7 emu/g, and 9.1 emu/g at 5 K (Figure 5c, insets). The small change in the coercivity (47 Oe) over the entire temperature range (395 K) is
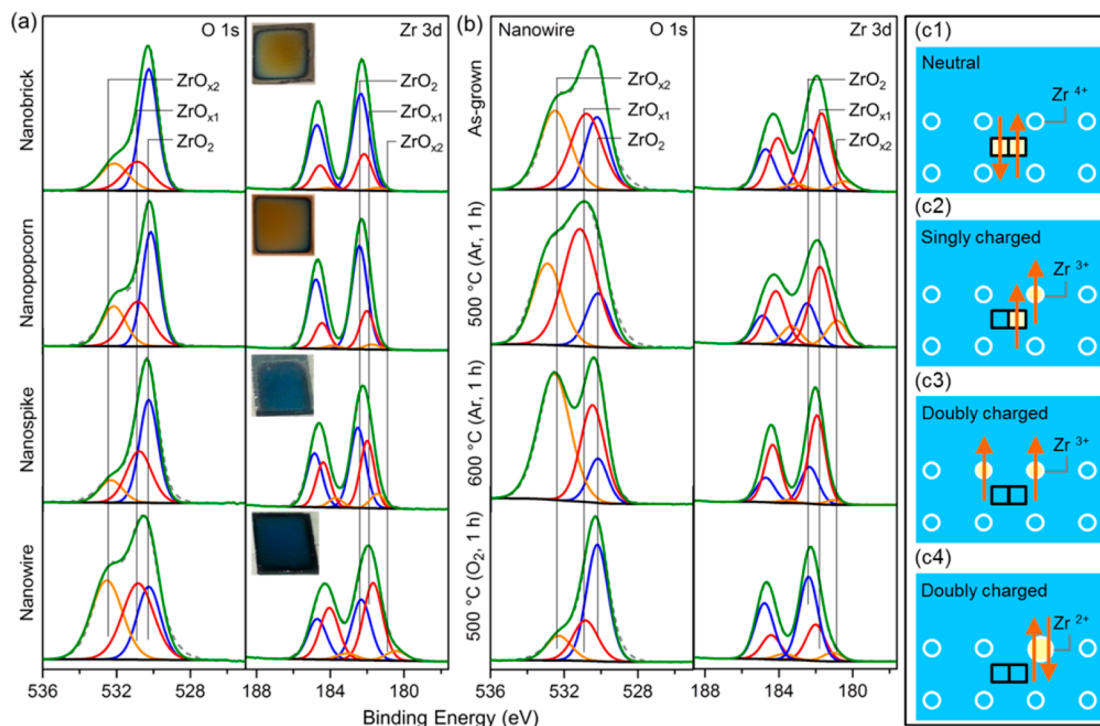
Figure 6. (a) XPS spectra of Zr 3d, and O 1s regions of (a) as-deposited ZrO_2 nanostructured films, and (b) ZrO_2 nanowire films as-deposited and postannealed under different conditions. In addition to the ZrO_2 features, two sets of defect features corresponding to ZrO_{x1} ($2 > x1 > 1.5$) and ZrO_{x2} ($1.5 \geq x2 > 1$) are used to fit the residual intensities. The minor changes in the peak positions (and widths) of these defect features from the marked positions correspond to the changes in the defect distributions within the considered $x1$ and $x2$ ranges. Photographs of the as-grown nanostructured samples are shown as insets in (a). (c1−c4) Schematic representations of three plausible types of oxygen vacancies in ZrO_2. The Zr^{4+} ions are marked by open white circles, and only the Zr^{3+} and Zr^{2+} ions [i.e., with relocation of electrons (with spin up and spin down as represented by up and down arrows, respectively) from the oxygen-vacancy defect sites] are shown as solid circles. In the interest of clarity, oxygen atoms are not shown, and the oxygen vacancy sites are marked as open squares.

characteristic of dilute ferromagnetism (Figure 5c), which affirms that PLD-grown defect-rich ZrO_2 nanowires exhibit the distinctive ferromagnetic order of TDFSOs. In addition, we have used Arrott plot (Figure S2a) and the power law (Figure S2b) to estimate the Curie temperature (T_C).[26] As shown in Figure S2b, the model provides an excellent fit (solid line) to the experimental results (open circles), and the T_C for the as-grown ZrO_2 nanowires is determined to be 700 K. Similarly, T_C for ZrO_2 nanospikes, nanopopcorns, and nanobricks are found to be 650, 550, and 400 K, respectively (Figure S3).

We perform zero-field-cooled and field-cooled magnetization measurements for the ZrO_2 nanowires at an applied field of 100 Oe between 1.8 and 400 K (Figure 5d). The wide separation of the zero-field-cooled and field-cooled magnetization curves over the entire temperature range suggests irreversibility of susceptibilities. The magnetic moments also do not drop to zero, indicating a high T_C above 400 K, in good agreement with the Arrott plot shown in Figure S2a. Since the zero-field-cooled magnetization appears to increase linearly with increasing temperature without any obvious peak, these ZrO_2 nanowires exhibit typical ferromagnetic behavior without any blocking temperature below 400 K. The absence of blocking temperature within this temperature range therefore confirms that ferromagnetism of the nanowires is of intrinsic origin and is not caused by extrinsic effects[27] such as those arising from the presence of ferromagnetic impurities or dopants. In addition, the extrapolated T_C from the model is found to be in excellent accord with the Curie temperature determined from separate magnetization measurement carried out to 950 K, with the

sharp decrease of magnetization at 700 K confirming the Curie temperature of ZrO_2 nanowire sample (Figure S2c).

Origin of Ferromagnetism in Undoped ZrO_2 Nanostructures. Recent studies have suggested that point defects, such as oxygen vacancies, could stabilize the tetragonal phase of ZrO_2, providing the key to understand the origin of the observed room-temperature ferromagnetic behavior in undoped ZrO_2.[13,25] To date, ferromagnetism has only been observed predominantly in tetragonal ZrO_2.[13] For a mixture of monoclinic and cubic phases of ZrO_2, the interfacial defects in the grain boundary region have, however, been suggested to play an important role in generating ferromagnetic order in undoped ZrO_2.[28] There is, therefore, no consensus on the defect origin of room-temperature ferromagnetism in undoped ZrO_2. Furthermore, room-temperature ferromagnetism is often observed only in postannealed thin film and powders of TDFSO nanostructures, and it has been found to exhibit notable surface-dependent effects,[29] particularly those related to surface defects.[30,31]

In order to determine the origin of ferromagnetism, we perform X-ray photoelectron spectroscopy (XPS) study of the as-grown ZrO_2 nanostructure samples (Figure 6). A representative survey spectrum of ZrO_2 nanowires shows the presence of only Zr, O, Au, and C (Figure S4). More importantly, the absence of Mn 2p at 638.3 eV, Fe 2p at 706.8 eV, and Co 2p feature at 779.4 eV (binding energy) allows us to rule out any contamination caused by unwanted magnetic impurities in the sample. The prominent Zr $3d_{5/2}$ peak at 182.4 eV corresponds to the Zr^{4+} state for ZrO_2, while the residual

Table 1. Comparison of the Estimated Specific Surface Area, Percentages of the Monoclinic and Tetragonal Phases, Percentages of the Zr 3d and O 1s Peak Intensities for Defect-Related Features (ZrO_{x1}, ZrO_{x2}, and Their Sums), and the Saturated Magnetization (Ms), Remanence (Mr) and Coercivity (Hc) Measured at Room Temperature for the ZrO_2 Nanostructured Films As-Deposited at the Specified Temperature and for ZrO_2 Nanowire Films upon Various Post-Treatments

| | | XRD[b] | | XPS[c] (%) | | | | | | magnetic properties | | |
| | | | | Zr 3d | | | O 1s | | | | | |
ZrO_2 nanostructured film	estimated specific surface area (nm^{-1})[a]	monoclinic (%)	tetragonal (%)	ZrO_{x1}	ZrO_{x2}	ZrO_{x1} + ZrO_{x2}	ZrO_{x1}	ZrO_{x2}	ZrO_{x1} + ZrO_{x2}	M_S (emu/g)	M_r (emu/g)	Hc (Oe)
Nanobrick, 550−770 °C	0.05	0	100	21.9	2.1	24.0	20.9	17.6	37.5	0.6	0.1	50
Nanopopcorn, 550 °C	0.08	32	68	22.9	2.8	25.7	28.7	22.9	51.6	1.2	0.3	73
Nanospike, 650 °C	0.11	57	43	32.2	8.3	40.5	31.6	15.5	47.1	2.9	0.5	77
Nanowire, 770 °C (as-grown)	0.13	75	25	49.3	7.4	56.7	36.5	37.1	73.6	5.9	1.5	99
Nanowire (500 °C, Ar, 1 h)				55.5	16.2	71.7	54.1	32.4	86.5	7.3	2.3	113
Nanowire (600 °C, Ar, 1 h)				69.4	2.7	72.1	31.9	55.9	87.8	3.2	0.6	71
Nanowire (500 °C, O$_2$, 1 h)				24.3	7.7	32.0	26.6	14.7	41.3	1.6	0.2	54

[a]Only the exposed surface area of an "ideal" nanostructure of the specific shape and size is considered in the calculation, with details given in the Table S1 (Supporting Information). [b]The relative phase percentages are obtained from the peak intensities of monoclinic (−111) and tetragonal (101) features using the X-pert HighScore software assuming random orientations. [c]The percentages of individual components are calculated by dividing the peak area of that component with the total contribution of ZrO_2 + ZrO_{x1} + ZrO_{x2}.

intensity between the Zr^{4+} feature (at 182.4 eV) and metallic Zr^0 feature (at 178.3 eV) could be generally fitted to two components: ZrO_{x1} ($2 > x1 > 1.5$) and ZrO_{x2} ($1.5 \geq x2 > 1$) (Figure 6a). The prominent O 1s peak located at 530.3 eV is attributed to O^{2-} in ZrO_2, while the residual O 1s intensity between 532.3 and 530.9 eV can be assigned to oxygen anions in the oxygen-deficient ZrO_{x1} and ZrO_{x2} species within the matrix. These results therefore suggest that PLD-grown ZrO_2 nanostructures are highly oxygen-deficient and the observed magnetization could be correlated with the oxygen vacancy defects.

Earlier density function theory (DFT) calculations have shown that excess electrons in oxygen-deficient ZrO_2 experience an attractive Madelung potential (as in MgO), which results into three favored charge states of oxygen vacancies.[17] Accordingly, we have therefore classified the overall oxygen vacancy concentration to consist of neutral, singly charged, and doubly charged defect contributions (Figure 6c). The formation of a singly charged oxygen vacancy would produce one electron in the singly charged oxygen vacancy site, with the other electron in the corresponding Zr atom leading to a Zr^{3+} ($4d^1$) ion (Figure 6c2). For the doubly charged oxygen vacancy, the two electrons from the vacancy site could be located at two nearest-neighbor Zr ions leading to two Zr^{3+} ($4d^1$) ions (Figure 6c3), or at one single Zr atom leading to a Zr^{2+} ($4d^2$) ion (Figure 6c4). For the neutral oxygen vacancy, the two electrons remain at the oxygen vacancy site and there is therefore no apparent effect on the Zr^{4+} ion (Figure 6c1).

The existence of trapped electrons also changes the colors of the as-deposited samples. Evidently, the sample color has changed from light golden (nanobrick) to dark golden (nanopopcorn) to light blue (nanospike), and to deep blue (nanowire), due to the increasing amount of oxygen vacancy concentrations within the nanostructures (Figure 6a, insets). The corresponding reflectance spectra follow essentially the same "exponential-like" profile over the 300−600 nm range, with the magnitude following the descending trend: nanobricks > nanopopcorns > nanospikes > nanowires, and the absorbance following the opposite trend (Figure S5). The absorbance of the ZrO_2 nanostructures in the visible region could therefore be

attributed to the existence of defect states within the bandgap, the overlapping and hybridization of which lead to impurity bands within the band gap.[32] Moreover, these defect-rich ZrO_2 samples retain their individual color profiles upon storage in ambient atmosphere for over a year, indicating that the oxygen vacancy defects are located in the bulk and not just at the surface of these nanostructures.

The different extents of lattice relaxation associated with these differently charged oxygen vacancies change the corresponding O 1s and Zr 3d binding energies in oxygen-deficient ZrO_2. The decrease in electron charge density for the $O-Zr^{3+}$ bond (relative to the $O-Zr^{4+}$ bond) results in less screening of the O 1s electrons, which consequently increases the effective nuclear charge. This leads to an increase in the O 1s binding energy and correspondingly a decrease in the Zr 3d binding energy. The O 1s peaks of ZrO_{x1} and ZrO_{x2} therefore correspond to the singly- and doubly charged oxygen vacancies, respectively, while the neutral oxygen vacancy defect peak likely lies at or near the same position of the ZrO_2 peak. As the binding energy of Zr 3d peak of ZrO_{x2} is farther away from the metallic Zr, and the relative intensities (and concentrations) of O 1s and Zr 3d in ZrO_{x2} are significantly different from those in ZrO_{x1}, the doubly charged oxygen vacancies are expected to lead to predominantly Zr^{3+} ions (Figure 6c3) instead of Zr^{2+} ions (Figure 6c4). Along with the minor differences in the binding energy positions and in the full widths at half maximum, the discernible intensity variations found for the O 1s and Zr 3d states for the ZrO_{x1} and ZrO_{x2} components therefore reflect the differences in the relative composition of these different types of oxygen vacancies in a particular sample. The O 1s and the Zr 3d intensity percentages for the ZrO_{x1} and ZrO_{x2} components of the respective total intensities [i.e., $ZrO_2+ZrO_{x1} + ZrO_{x2}$] for the nanostructures are summarized in Table 1. For ZrO_{x1} [and the total defect intensity, neutral and ($ZrO_{x1} + ZrO_{x2}$)], the Zr 3d percentages appear to follow the descending trend: nanowire > nanospike > nanopopcorn ≅ nanobrick. The O 1s percentages for ZrO_{x1} follow the trend: nanowire ≅ nanospike > nanopopcorn > nanobrick, while there appear no clear patterns in the Zr 3d and O 1s percentages for ZrO_{x2}.

To further clarify the role of the types of oxygen vacancy defects in determining the magnetic property, we carry out annealing experiments in an oxygen or Ar atmosphere at different temperatures (500 and 600 °C) for the as-deposited ZrO_2 nanowires. X-ray diffraction analysis shows that there is no discernible change in the relative composition of the crystalline phases in the nanowires caused by these postannealing treatments, regardless of the annealing temperature and environment. However, postannealing the as-grown ZrO_2 nanowires in Ar at 500 °C increases the amount of oxygen vacancy defects (Figure 6b). As expected, the proportions of the types (i.e., the relative compositions) of oxygen vacancies corresponding to the ZrO_{x1} and ZrO_{x2} features have discernibly increased. Further postannealing the sample at 600 °C in Ar has increased the total oxygen vacancies (related to ZrO_{x1} + ZrO_{x2}), but the overall full-width half-maximum of the Zr 3d peak has decreased significantly, and the O 1s and Zr 3d peaks corresponding to ZrO_{x1} are slightly shifted to the lower and higher binding energy, respectively, all with respect to the as-grown features (Figure 6b, Table 1). These results therefore suggest that postannealing at 600 °C produces highly reduced ZrO_2 and favors the formation of more neutral oxygen vacancies than the as-grown and 500 °C Ar-annealed samples. For the ZrO_2 nanowires postannealed in O_2, we expect a significant decrease in the amount of oxygen vacancy defects, and this is indeed supported by the large reduction in the composition for the ZrO_{x1} and ZrO_{x2} XPS features (Figure 6b, Table 1). The changes in the defect types and its relative proportions caused by the post-treatments are found to greatly affect the magnetic properties. Indeed, Figure 5b shows that the reduction in the amounts of oxygen vacancies significantly decreases the saturation magnetization of the nanowires O_2-annealed at 500 °C. Furthermore, the saturation magnetization for the 500 °C Ar-annealed nanowires has increased but that for the 600 °C Ar-annealed sample has decreased significantly, due to the increase in neutral oxygen vacancies in the 600 °C Ar-annealed sample. These results therefore suggest that both the types (singly charged, and doubly charged, and neutral oxygen vacancies) and relative amounts of these oxygen vacancy defects play a crucial role for the observed room-temperature ferromagnetic behavior in undoped ZrO_2 nanowires.

In Table 1, we compare the estimated specific surface areas (i.e., surface area-to-volume ratios) of individual nanostructures (Table S1), the relative percentages of ZrO_2 monoclinic and tetragonal phases as obtained from the XRD patterns (Figure 3), the relative compositions of oxygen vacancy defects as determined from the Zr 3d and O 1s XPS spectra (Figure 6), and the saturation magnetization and coercivity of the ZrO_2 nanostructures (Figure 5). The relations among these observed properties reveal several important features about the observed ferromagnetism. First, the saturation magnetization increases with increasing relative amount of the monoclinic phase. However, the magnetization remains nonzero even when there is only tetragonal phase as in the nanobrick film, which shows that the magnetization is not exclusive to the monoclinic or tetragonal phase. Second, the presence of different charge states of oxygen vacancies (i.e., singly charged, doubly charged, and neutral oxygen vacancies) enables both M_S and H_C to be tunable by manipulating their relative amounts, indicating that the relative compositions and not just the total amounts of these oxygen vacancy defects are important. Lastly, the observed ferromagnetism exhibits morphology (i.e., shape)

dependency. As the surface usually contains more defects than the bulk, their relative amounts can be modulated by manipulating the specific surface areas, as dictated by the morphology of the nanostructures. As the types and amounts of oxygen vacancy defects are related to the specific surface area (surface defects) and growth temperature in an oxygen-deprived environment (bulk defects) of the nanostructure, the larger saturation magnetization and coercivity are found for the nanowires with higher estimated specific surface area and higher growth temperature (0.13 nm^{-1}, 770 °C) than nanospikes (0.11 nm^{-1}, 650 °C), nanopopcorns (0.08 nm^{-1}, 550 °C), and nanobricks (0.05 nm^{-1}, 770 °C) (Table 1). The observed magnetization is therefore consistent with the relative amounts of different charge states of oxygen vacancies (neutral, singly charged, and doubly charged vacancies), with the singly charged and doubly charged oxygen vacancies contributing more to magnetization than the neutral oxygen vacancies in which cancellation of paired electron spins occur. This insight could also be applied to understanding the manifestation of d^0 ferromagnetism in low-dimensional nanostructures or thin films with high specific surface areas.

Proposed Model for Ferromagnetism in Defect-Rich Undoped TDFSOs. There have been a few theoretical studies[19,33−35] on the origin of ferromagnetism in TDFSOs. In the very first model of TDFSOs, the Heisenberg model, the d electrons of the dopant (transition metal cations) are well localized, and they couple with one another ferromagnetically via long-range-ordered interactions among the free carriers (2p holes or 4s electrons).[36] Given the small amount of the dopants (a few percent), however, it is difficult to conceive how the exchange interaction could occur over a large separation between localized moments. Contrary to the Heisenberg model, the observed magnetization has already been reported to be independent of the dopant concentration,[11,12] which suggests that the Ruderman-Kittel-Kasuya-Yosida interaction may not be the main cause of ferromagnetism in TDFSOs. In the so-called bound magnetic polaron model, the defects in doped-TDFSOs are taken into account. The ferromagnetic coupling is mediated by shallow donor electrons associated with defects via exchange interactions with the localized d electrons of the dopants.[7] However, this model still cannot explain how T_C in dilute ferromagnetic semiconductor oxides can be so high (i.e., well above room temperature) or how semiconducting oxides without any transition metal dopants (i.e., without any unpaired d electrons) can be ferromagnetic. Very recently, a charge-transfer ferromagnetism model has been proposed as an extension to the bound magnetic polaron model.[16] This model assumes that the presence of defects introduces an impurity band, and the presence of dopants provides a charge reservoir in the system to facilitate hopping of electrons to or from the impurity band, which leads to splitting of spin states.[16] This model, however, cannot explain how ferromagnetism could occur in undoped TDFSOs, because there is no charge reservoir due to the absence of dopants. Meanwhile, experiments using X-ray magnetic circular dichroism have revealed that the dopant (Co 3d, Mn 3d, and Cr 3d) sublattice is paramagnetic at all temperature down to 2 K, both at the surface and in the bulk of the films.[11,12] As the dopants are evidently not the origin of ferromagnetism, ferromagnetism in doped semiconducting oxide thin films must therefore be related to defects.

We hypothesize that narrow impurity bands could form below the conduction band minimum as a result of the overlap
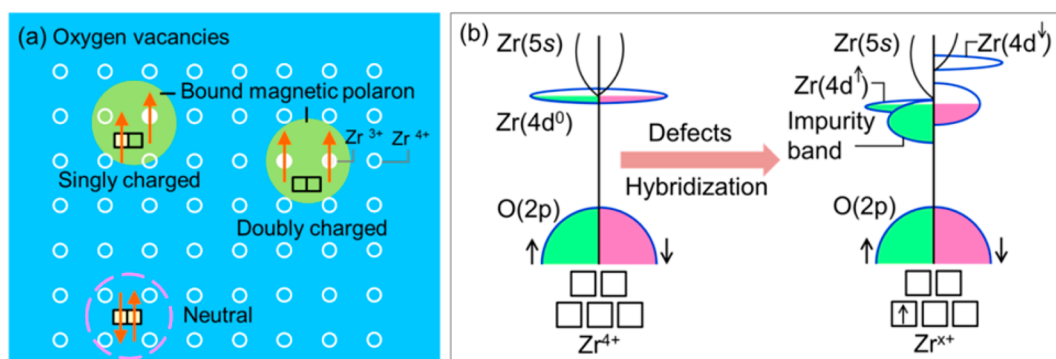
Figure 7. (a) Formation of bound magnetic polarons (marked by light green circles) by singly charged and doubly charged oxygen vacancies. The Zr^{4+} ions are marked by open white circles, while the Zr^{3+} ions are shown as solid white circles. In the interest of clarity, oxygen atoms are not shown, and the oxygen vacancy sites are marked by open white squares. The neutral oxygen vacancy site is highlighted by open dashed circle. The arrows indicate the direction of the spins. (b) Schematic representations of the proposed defect-induced bound polaron model for ferromagnetism in undoped ZrO_2 nanostructures containing oxygen vacancies and mixed-valence of Zr ions. This mechanism involves formation of an impurity band and its overlapping with Zr 4d states leading to ferromagnetic exchange coupling.

and hybridization of the defect states associated with different charge states of the oxygen vacancies.[37] In ZrO_2, formation of a singly charged oxygen vacancy would therefore result in one electron in the singly charged oxygen vacancy site, with the other electron in the corresponding Zr atom leading to a Zr^{3+} ($4d^1$) ion. In such a system, either the singly charged oxygen vacancy or the Zr^{3+} ($4d^1$) ion with one unpaired electron can effectively behave as a localized electron, similar to the unpaired d electrons of a dopant in doped-TDFSOs as proposed in earlier models. When these localized electrons are coupled with the conduction band electrons, the conduction band electrons became spin-polarized around the localized spins. Given that the stronger form of ferromagnetism usually requires localized rather than itinerant electrons, we would expect ferromagnetic exchange interactions to occur between the singly charged oxygen vacancy electron and the $4d^1$ electron because the spins of all the carriers could assume the same direction. The parallel orientation of both localized spins therefore leads to the formation of a bound magnetic polaron at or near the defect site (Figure 7a), which causes both the conduction band and impurity band to split apart into a spin-up and a spin-down bands due to the difference in potential energies for the spin-up and spin-down electrons (Figure 7b). Since the Fermi level is identical to both spin-up and spin-down bands, there is a small surplus of the type of spin in the resulting lower band (Figure 7b). This is in contrast to defect-free TDFSOs, in which an equal amount of spin-up and spin-down electrons would give rise to paramagnetic response (Figure 7b).[38] Similarly, a doubly charged oxygen vacancy would result in the relocation of these electrons to two nearest neighboring Zr atoms, leading to formation of two Zr^{3+} ($4d^1$) ions (Figure 7a). The exchange interactions of these two d-electrons with each other and with the free carriers (electrons) could also lead to bound magnetic polaron formation and splitting of energy levels of the impurity band around the vacancy defect. On the other hand, the antiparallel electron spins of the neutral oxygen vacancies could only mediate weak antiferromagnetic exchange interactions due to cancellation of the paired electron spins (Figure 7a). However, due to the quantum confinement effect in low-dimensional nanostructures, the neutral oxygen vacancies that have a triplet ground state or a low-lying triplet excited state could overlap to form a narrow impurity band and can be polarized by exchange with empty Zr 4d states.[39] This is not

supported by our XPS and magnetization data of the 600 °C Ar-annealed nanowire sample, which show that contribution from the neutral oxygen vacancies to the total ferromagnetism is negligibly small. Moreover, the Curie temperature depends on the degree of hybridization, which corresponds to charge transfer from a donor-derived impurity band (oxygen vacancy) to the unoccupied d states at the Fermi level.[7] The variation of the donor concentrations, i.e., compositions of the oxygen vacancy defects in the present case, could therefore change the T_C of the nanostructures. The higher T_C observed for the ZrO_2 nanowires, relative to those of nanobricks, nanopopcorns, and nanospikes, could therefore be attributed to the higher concentrations of singly charged and doubly charged oxygen vacancies in the nanowires.

Our proposed model, as depicted in Figure 7, can be generally applicable to a wide range of undoped TDFSOs The concept of impurity band formation and its hybridization with empty d states in undoped oxides suggests that magnetic ordering in semiconductor oxides could in principle be achieved by using different types of anion vacancy defects in the host lattice. In a separate study, we have indeed observed similar morphology and defect-dependent ferromagnetism in defect-rich, dopant-free TiO_2 nanostructures. In particular, the magnetization in TiO_2 nanostructures is found to increase with increasing amounts and relevant types of oxygen vacancy defects within the nanostructures: nanobricks < nanobelts < corrugated nanowires < straight nanowires < decorated nanowires (not shown).

These results therefore provide new insight into and better mechanistic understanding of ferromagnetism in oxygen vacancy defect-rich undoped TDFSOs. More importantly, our defect-rich ZrO_2 nanostructured films are novel, because our nanostructured samples require only 2000 Oe external field to reach saturation, making them the most responsive materials with the highest sensitivity to the external field reported to date. The observed saturation magnetization of our nanowire sample (5.9 emu/g) is significantly higher than those reported for undoped ZrO_2 (0.18 emu/g)[13] and Mn-doped ZrO_2 (0.02 emu/g)[40] thin films, undoped ZnO (0.4 emu/g)[14] and Mn-doped ZnO (0.05 emu/g)[41] thin films, undoped ZnO nanoparticulate film (0.003 emu/g),[42] and $Ag_{1.2}V_3O_8$ nanorings (0.002 emu/g),[43] all of which were obtained with considerably higher applied magnetic field. Indeed, the saturation magnet-

ization of our ZrO_2 nanowire film is also significantly higher than other nanostructured films, including ~26 times higher than the nanoporous pure TiO_2 nanoribbon film[44] and Cu-doped ZnO nanowire film (both 0.2 emu/g);[45] and over 80 times higher than Fe and N codoped TiO_2 nanorods (0.06 emu/g),[46] Cr-doped TiO_2 nanorods (0.07 emu/g),[47] transition metal-doped mesoporous In_2O_{3-y} (0.03 emu/g),[48] and V-doped TiO_2 nanotubes (0.008 emu/g).[49] These results therefore demonstrate that our as-grown ZrO_2 nanowire sample has the best magnetization reported to date and they also present viable opportunities for future applications of this new class of defect-rich nanomaterials in spin-based technologies.

CONCLUSION

In summary, the use of a high vacuum system and precise control of the growth temperature and environment have enabled us to produce, for the first time, defect-rich, dopant-free nanostructured films with different compositions of oxygen vacancy defects. Independent of the phase of ZrO_2 (tetragonal or monoclinic), it is the amounts and types of oxygen vacancy defects of the nanostructure that control the ferromagnetic property of ZrO_2. The observed magnetization (5.9 emu/g) is not only significantly greater than other ZrO_2 nanomaterials reported to date, but also at least an order of magnitude higher than the magnetization reported for other doped and undoped TDFSOs. We hypothesize a new defect-induced bound polaron model for the defect-rich undoped TDFSOs, which is generally applicable to other undoped TDFSO systems.

In marked contrast to most of the TDFSO samples reported in the literature, all of which required post-treatment (such as annealing in a reductive environment) or doping with secondary materials, the present ZrO_2 nanowires are prepared with one distinct advantage, i.e., without the need for any postsynthesis modification or treatment. The present facile synthesis process makes the fabrication of these defect-rich, dopant-free ZrO_2 nanostructured films easily scalable. Furthermore, our magnetization values (Table 1) are estimated based on the sample volume, with the assumption that the nanostructures are tightly packed and densely distributed over the entire sampling area. If we consider that the nanowires only occupy ~20% of the presumed sample volume (Figure 1e2), the saturation magnetization could be ~5 times greater, making the magnetization reported here (29.5 emu/g for as-grown ZrO_2 nanowires) even greater. Indeed, the packing density and the overall amount of the nanowires could be greatly enhanced physically by increasing the areal density of the nanowires (e.g., by increasing the GNI density) and/or the length of the nanowires (e.g., by increasing the deposition time).

More importantly, as T_C found for the as-grown ZrO_2 nanowires (700 K) is significantly higher than room temperature, the nanostructured film can be readily incorporated into the fabrication protocol of room-temperature spin-based electronic devices that employ spins as the information carriers. For example, the present dopant-free, defect-rich ZrO_2 nanostructured films could be used to build more efficient spin transistors[50] and spin-based logic circuits[51] that could operate well above room temperature by taking advantage of their high saturated magnetization and high T_C capabilities. The high optical absorption property of these defect-rich nanomaterials also promises more efficient solar-driven spin devices,[52] in which the generation of spin currents by visible sunlight opens new door to solar-driven magneto-electronics. Furthermore, fabricating hybrid and/or core−shell nanowires with

a ferroelectric material would enable multiferroic (simultaneous ferroelectric and magnetic ordering) tunnel junction in a single nanowire, which could be used as a spin filter device with potential to be controlled both electrically and magnetically.[53] This can be easily accomplished by switching the targets (using a multitarget holder) during the growth of ZrO_2 nanowires. The present approach of intentionally growing defect-rich, dopant-free ZrO_2 nanostructures by catalyst-assisted PLD method could be extended to build other novel dilute ferromagnetic semiconductors that promise new spin-based applications.

■ ASSOCIATED CONTENT

Ⓢ Supporting Information
The Supporting Information is available free of charge on the ACS Publications website at DOI: 10.1021/jacs.6b06949.

Figures S1−S5, Table S1 (PDF)

■ AUTHOR INFORMATION

Corresponding Author
*tong@uwaterloo.ca

Notes
The authors declare no competing financial interest.

■ ACKNOWLEDGMENTS

■ REFERENCES

(1) Fert, A. *Angew. Chem., Int. Ed.* **2008**, *47*, 5956−5967.
(2) Furdyna, J. K. *J. Appl. Phys.* **1988**, *64*, R29−R64.
(3) Lee, J.; Oszwałdowski, R.; Gøthgen, C.; Žutić, I. *Phys. Rev. B: Condens. Matter Mater. Phys.* **2012**, *85*, 045314.
(4) Rangaraju, N.; Peters, J. A.; Wessels, B. W. *Phys. Rev. Lett.* **2010**, *105*, 117202.
(5) Dietl, T. *Nat. Mater.* **2010**, *9*, 965−974.
(6) Žutić, I.; Fabian, J.; Sarma, S. D. *Rev. Mod. Phys.* **2004**, *76*, 323−410.
(7) Coey, J. M. D.; Venkatesan, M.; Fitzgerald, C. B. *Nat. Mater.* **2005**, *4*, 173−179.
(8) Philip, J.; Punnoose, A.; Kim, B. I.; Reddy, K. M.; Layne, S.; Holmes, J. O.; Satpati, B.; LeClair, P. R.; Santos, T. S.; Moodera, J. S. *Nat. Mater.* **2006**, *5*, 298−304.
(9) Bonanni, A.; Dietl, T. *Chem. Soc. Rev.* **2010**, *39*, 528−539.
(10) Jit, S.; Weerasekara, A. B.; Jayasinghe, R. C.; Matsik, S. G.; Perera, A.; Buchanan, M.; Sproule, G. I.; Liu, H. C.; Stintz, A.; Krishna, S.; Khanna, S. P.; Lachab, M.; Linfield, E. H. *IEEE Electron Device Lett.* **2008**, *29*, 1090−1093.
(11) Barla, A.; Schmerber, G.; Beaurepaire, E.; Dinia, A.; Bieber, H.; Colis, S.; Scheurer, F.; Kappler, J.; Imperia, P.; Nolting, F.; Wilhelm, F.; Rogalev, A.; Muller, D.; Grob, J. J. *Phys. Rev. B: Condens. Matter Mater. Phys.* **2007**, *76*, 125201.
(12) Hong, N. H.; Baria, A.; Sakai, J.; Huong, N. Q. *Phys. Status Solidi C* **2007**, *4*, 4461−4466.
(13) Ning, S.; Zhang, Z. *RSC Adv.* **2015**, *5*, 3636−3641.
(14) Zhan, P.; Wang, W.; Liu, C.; Hu, Y.; Li, Z.; Zhang, Z.; Zhang, P.; Wang, B.; Cao, X. *J. Appl. Phys.* **2012**, *111*, 033501.
(15) Matsumoto, Y.; Murakami, M.; Shono, T.; Hasegawa, T.; Fukumura, T.; Kawasaki, M.; Ahmet, P.; Chikyow, T.; Koshihara, S.; Koinuma, H. *Science* **2001**, *291*, 854−857.
(16) Coey, J. M. D.; Wongsaprom, K.; Alaria, J.; Venkatesan, M. *J. Phys. D: Appl. Phys.* **2008**, *41*, 134012.
(17) Ganduglia-Pirovano, M. V.; Hofmann, A.; Sauer, J. *Surf. Sci. Rep.* **2007**, *62*, 219−270.

(18) Hong, N. H.; Park, C.; Raghavender, A. T.; Ciftja, O.; Bingham, N. S.; Phan, M. H.; Srikanth, H. *J. Appl. Phys.* **2012**, *111*, 07C302.

(19) Maca, F.; Kudrnovsky, J.; Drchal, V.; Bouzerar, G. *Appl. Phys. Lett.* **2008**, *92*, 212503.

(20) Javey, A.; Kim, H.; Brink, M.; Wang, Q.; Ural, A.; Guo, J.; McIntyre, P.; McEuen, P.; Lundstrom, M.; Dai, H. *Nat. Mater.* **2002**, *1*, 241−246.

(21) Ohmi, T. *J. Electrochem. Soc.* **1996**, *143*, 2957−2964.

(22) Wagner, R. S.; Ellis, W. C. *Appl. Phys. Lett.* **1965**, *4*, 89.

(23) Chang, J.; Young, T.; Yang, Y.; Ueng, H.; Chang, T. *Mater. Chem. Phys.* **2004**, *83*, 199−203.

(24) Massalski, T. B.; Okamoto, H.; Abriata, J. P. *Bull. Alloy Phase Diagrams* **1985**, *6*, 519−521.

(25) Ning, S.; Zhan, P.; Xie, Q.; Li, Z.; Zhang, Z. *J. Phys. D: Appl. Phys.* **2013**, *46*, 445004.

(26) Xiu, F.; Wang, Y.; Kim, J.; Hong, A.; Tang, J.; Jacob, A. P.; Zou, J.; Wang, K. L. *Nat. Mater.* **2010**, *9*, 337−344.

(27) van der Meulen, M. I.; Petkov, N.; Morris, M. A.; Kazakova, O.; Han, X.; Wang, K. L.; Jacob, A. P.; Holmes, J. D. *Nano Lett.* **2009**, *9*, 50−56.

(28) Wang, D. D.; Qi, N.; Jiang, M.; Chen, Z. Q. *Appl. Phys. Lett.* **2013**, *102*, 042407.

(29) Li, T.; Ong, C. S.; Herng, T. S.; Yi, J. B.; Bao, N. N.; Xue, J. M.; Feng, Y. P.; Ding, J. *Appl. Phys. Lett.* **2011**, *98*, 152505.

(30) Sundaresan, A.; Bhargavi, R.; Rangarajan, N.; Siddesh, U.; Rao, C. N. R. *Phys. Rev. B: Condens. Matter Mater. Phys.* **2006**, *74*, 161306R.

(31) Panigrahy, B.; Aslam, M.; Misra, D. S.; Ghosh, M.; Bahadur, D. *Adv. Funct. Mater.* **2010**, *20*, 1161−1165.

(32) Hildebrandt, E.; Kurian, J.; Mller, M. M.; Schroeder, T.; Kleebe, H. J.; Alff, L. *Appl. Phys. Lett.* **2011**, *99*, 112902.

(33) Das Pemmaraju, C.; Sanvito, S. *Phys. Rev. Lett.* **2005**, *94*, 217205.

(34) Rahman, G.; García-Suárez, V. M.; Hong, S. C. *Phys. Rev. B: Condens. Matter Mater. Phys.* **2008**, *78*, 184404.

(35) Maca, F.; Kudrnovsky, J.; Drchal, V.; Bouzerar, G. *Appl. Phys. Lett.* **2008**, *92*, 212503.

(36) Dietl, T. *Science* **2000**, *287*, 1019−1022.

(37) Foster, A. S.; Sulimov, V. B.; Lopez Gejo, F.; Shluger, A. L.; Nieminen, R. M. *Phys. Rev. B: Condens. Matter Mater. Phys.* **2001**, *64*, 224108.

(38) Hong, N. H.; Sakai, J.; Poirot, N.; Brizé, V. *Phys. Rev. B: Condens. Matter Mater. Phys.* **2006**, *73*, 132404.

(39) Stoneham, A. M. *Theory of Defects in Solids*; Oxford University Press, Oxford, 1975.

(40) Zippel, J.; Lorenz, M.; Setzer, A.; Wagner, G.; Sobolev, N.; Esquinazi, P.; Grundmann, M. *Phys. Rev. B: Condens. Matter Mater. Phys.* **2010**, *82*, 125209.

(41) Sharma, P.; Gupta, A.; Rao, K. V.; Owens, F. J.; Sharma, R.; Ahuja, R.; Guillen, J. M. O.; Johansson, B.; Gehring, G. A. *Nat. Mater.* **2003**, *2*, 673−677.

(42) Xu, X.; Xu, C.; Dai, J.; Hu, J.; Li, F.; Zhang, S. *J. Phys. Chem. C* **2012**, *116*, 8813−8818.

(43) Wu, C.; Zhu, H.; Dai, J.; Yan, W.; Yang, J.; Tian, Y.; Wei, S.; Xie, Y. *Adv. Funct. Mater.* **2010**, *20*, 3666−3672.

(44) Santara, B.; Giri, P. K.; Imakita, K.; Fujii, M. *Nanoscale* **2013**, *5*, 5476−5488.

(45) Wan, W.; Huang, J.; Zhu, L.; Hu, L.; Wen, Z.; Sun, L.; Ye, Z. *CrystEngComm* **2013**, *15*, 7887.

(46) Wang, H.; Wei, J.; Xiong, R.; Shi, J. *J. Magn. Magn. Mater.* **2012**, *324*, 2057−2061.

(47) Patel, S. K. S.; Gajbhiye, N. S. *J. Magn. Magn. Mater.* **2013**, *330*, 21−24.

(48) Pellicer, E.; Cabo, M.; Rossinyol, E.; Solsona, P.; Surinach, S.; Baro, M. D.; Sort, J. *Adv. Funct. Mater.* **2013**, *23*, 900−911.

(49) Patel, S. K. S.; Gajbhiye, N. S. *Solid State Commun.* **2011**, *151*, 1500−1503.

(50) Chang, L. Te; Wang, C. Y.; Tang, J.; Nie, T.; Jiang, W.; Chu, C. P.; Arafin, S.; He, L.; Afsal, M.; Chen, L. J.; Wang, K. L. *Nano Lett.* **2014**, *14*, 1823−1829.

(51) Dery, H.; Dalal, P.; Cywiński, Ł.; Sham, L. J. *Nature* **2007**, *447*, 573−576.

(52) Jansen, R. *Nat. Mater.* **2013**, *12*, 779−780.

(53) Ramesh, R.; Spaldin, N. A. *Nat. Mater.* **2007**, *6*, 21−29.